



High-Resolution Digital Image Correlation study of the strain localization during loading of a shot-peened RR1000 nickel-based superalloy

DOI:

[10.1016/j.actamat.2021.117306](https://doi.org/10.1016/j.actamat.2021.117306)

Document Version

Accepted author manuscript

[Link to publication record in Manchester Research Explorer](#)

Citation for published version (APA):

Orozco-caballero, A., Jackson, T., & Da Fonseca, J. Q. (2021). High-Resolution Digital Image Correlation study of the strain localization during loading of a shot-peened RR1000 nickel-based superalloy. *Acta Materialia*, [117306]. <https://doi.org/10.1016/j.actamat.2021.117306>

Published in:

Acta Materialia

Citing this paper

Please note that where the full-text provided on Manchester Research Explorer is the Author Accepted Manuscript or Proof version this may differ from the final Published version. If citing, it is advised that you check and use the publisher's definitive version.

General rights

Copyright and moral rights for the publications made accessible in the Research Explorer are retained by the authors and/or other copyright owners and it is a condition of accessing publications that users recognise and abide by the legal requirements associated with these rights.

Takedown policy

If you believe that this document breaches copyright please refer to the University of Manchester's Takedown Procedures [<http://man.ac.uk/04Y6Bo>] or contact uml.scholarlycommunications@manchester.ac.uk providing relevant details, so we can investigate your claim.



High-Resolution Digital Image Correlation study of the strain localization during loading of a shot-peened RR1000 nickel-based superalloy

Alberto Orozco-Caballero^{a,b,*}, Thomas Jackson^c and João Quinta da Fonseca^a

(^a) The University of Manchester, School of Materials, Manchester, M13 9PL, United Kingdom.

(^b) Now at: Department of Mechanical Engineering, Chemistry and Industrial Design, Polytechnic University of Madrid, 28012, Madrid, Spain.

(^c) Rolls-Royce plc, Derby, United Kingdom.

() Corresponding author: Alberto Orozco-Caballero, aorozcocaballero@gmail.com, alberto.orozco.caballero@upm.es +34 606 26 44 00.*

Abstract:

The improved crack nucleation resistance of shot-peened materials has been usually studied from the point of view of the residual compression stresses. Nevertheless, experimental limitations have made difficult to quantify strain localization during further deformation. In this study, we have used high-resolution digital image correlation (HRDIC) and electron backscatter diffraction (EBSD) in a large area covering shot-peened material and bulk to study quantitatively the strain distribution at the submicron scale. We found that, at the earlier deformation steps ($\epsilon < 2.5\%$), the slip intensity and distribution at the shot-peened region differ from that observed at the bulk. In the former, well-spaced, sharp and homogeneously distributed slip bands are observed. On the other

hand, in the shot-peened region, slip is less evident, and a more homogeneous diffuse deformation is observed along the majority of the grains. However, this region also contains a small number of slip bands that accumulate high strains, mainly along $\Sigma 3$ annealing twin boundaries. Additionally, the border between both regions, at a depth with no residual stresses, present the minimum strain values. During further deformation ($\epsilon > 2.5\%$), the strain distributions become similar along the material simultaneously to the residual stresses relaxation. A further analysis of the HRDIC maps allowed for the first time to quantify strain heterogeneity. This study reveals the importance of the local stress state and the strain history on the strain localization.

Keywords: Ni-base superalloy; shot-peening; digital image correlation; local strain distribution

1.- Introduction

Nickel-based superalloys are a group of superior alloys able to withstand aggressive service conditions. They are able to resist high-temperature fatigue and creep with a remarkable resistance to corrosion and oxidation [1]. Given this ability, both the air and land gas-turbine industries use these alloys extensively. In order to meet the demand for increased gas-turbine efficiency and superior damage tolerance, nickel-based superalloys are required to perform under higher stresses and operating temperatures. Among them, the γ' -strengthened polycrystalline RR1000 superalloy, developed by Rolls-Royce, is a high-performance alloy for operating in high-pressure compressor or turbine rotor discs. In order to avoid element segregation, RR1000 billets are obtained by consolidation of canned powder by hot isostatic pressing or hot compaction, followed by

extrusion. The final disc shape is obtained by isothermal forging and then solution treated. The RR1000 composition was defined to encourage damage tolerance and to increase the temperature capability over other conventional alloys, such as 720Li or Waspalloy [2]. Nevertheless, as for all metallic materials, nickel-based superalloys are prone to fatigue failure, at stresses which are nominally elastic, since plastic deformation can occur in a very localised sense, typically near sites of stress concentration. Usually, the fatigue damage is present most often in the form of intense, localised slip with the dislocation activity restricted to a small number of lattice planes [3].

In many components the required performance relies not only on the bulk microstructure, but also on their modification by processes such as shot-peening. The shot-peening process improves the endurance of components by preventing crack initiation as well as growth at the surface, which is the most common place for nucleation of fatigue cracks [4]. During shot-peening, small spherical media impinge on the surface of a material, producing plastic deformation in the near-surface microstructure [5]. This creates a work-hardened layer and a misfit strain between the bulk and surface of the material, causing an in-plane compressive residual stress state. The protective effect of shot-peening has been mainly attributed to these compressive stresses within the deformed layer that hinder crack propagation [6,7]. Nevertheless, despite of the general benefits of the shot-peening process, it can sometimes promote surface crack formation [8] and therefore, a precise control of the process is critically needed [9].

There are many publications studying the stress state on the different regions of a shot-peened material and their evolution with temperature and/or during mechanical loading, mainly because the experimental techniques for such studies are well established [10–15]. On the other hand, strain localization in the form of slip bands, persistent slip

bands (PSB) and deformation twins are commonly studied by means of different electron microscopy techniques. Such studies which are usually limited to small volumes of material and cannot quantify the plastic strain distribution ascribed to such features that leads to damage and limits the performance of shot-peened materials. As a result, we know relatively little about the strain localization behaviour of peened materials and how it interacts with the microstructure and the residual stress profile in peened surfaces. Improving our understanding of these effects, could help us refine peening treatments and improve component endurance under operation conditions.

The plastic strain distribution can be measured by means of digital image correlation (DIC). In DIC the displacement of a pattern in the sample surface at different deformation stages is used to calculate the strain distribution, usually with a spatial resolution ranging from millimetres to a few microns [16,17]. However, this resolution is not high enough to quantify the strain associated to different microstructural features, which are usually less than few microns in size. Recently, the development of surface patterning methods such as self-assembling of nanoparticles on the surface [18], electron beam lithography [19,20], deposition of Pt using FIB [21] and gold remodelling [22–29] have improved the achievable spatial resolution and high-resolution digital image correlation (HRDIC) can be used to measure strain at the submicron scale. Among this collection of patterning methods, the remodelling of a thin gold layer previously deposited on the sample surface is a versatile and simple method that provides one of the highest resolutions for extensive areas available to date [25,29–31]. The gold remodelling process provides a uniform, homogeneously distributed gold speckle pattern with typical speckle size in the range 20-150 nm. The resulting strain maps combine the benefits of

the high-resolution provided by such fine pattern with the coverage of large areas (by combining several images), typical of optical DIC measurements.

In this study, we present the results of the through-depth strain localization on a shot-peened RR1000 nickel-based superalloy with the aim of determining and quantify the plastic strain distribution of a shot peened sample tested at 400 °C. We performed correlations at six strain levels of uniaxial tension until failure in a remarkably large area of 950x420 μm^2 with a spatial resolution of ~ 330 nm. We found that the slip intensity and distribution at the shot-peened region differ from that observed at the bulk. While in the bulk well-spaced, sharp and homogeneously distributed slip bands are observed, in the shot-peened region the deformation is more homogeneous. Nevertheless, a small number of slip bands that accumulate high strain values are also present in this region. With increasing deformation, the strain distributions become similar for both regions. Nevertheless, a region at a depth of ~ 125 μm presents the lowest average strain values, particularly at the initial deformation steps. Previous studies showed that the maximum work-hardening is reached at this depth [14] suggesting that stress relaxation plays an important role on the observed plastic deformation distribution.

2.- Experimental procedure

2.1- Material

The material studied is the RR1000 nickel base superalloy provided by Rolls-Royce with the chemical composition indicated in Table 1. A block was shot-peened in the surface highlighted in red in the schematic of Fig. 1. The nozzle fired steel shot (ASH110) at 90° to the surface producing an almen intensity of 0.0065-0.0075” A (0.165-0.191mmA) and a coverage of 200%

Table1. Chemical composition of the RR 1000 alloy, wt.%.

Cr	Co	Mo	Al	Ti	Ta	Hf	Zr	C	B	Ni
14.35- 15.15	14- 19	4.25- 5.25	2.85- 3.15	3.45- 4.15	1.35- 2.15	0- 1	0.05- 0.07	0.012- 0.033	0.01- 0.025	bal

2.2- Microstructural characterization

We used Electron Backscattered Diffraction (EBSD) to characterize the microstructure in the transverse section of the shot-peened sample (area highlighted in green in the schematic of Fig. 1) with a CamScan MX2000 equipped with an Oxford Instruments EBSD camera operating at an acceleration voltage of 20 kV and using a step size of 0.45 μm . The sample was ground to #4000 grit paper and finished with OP-S (0.2 μm) suspension for ~ 30 min. EBSD data was analysed using the commercial Channel 5 software (Oxford Instruments). The raw EBSD data can be found in [32]

2.3- Mechanical characterization

A dog-bone tensile sample with 20 x 10 x 1 mm gauge dimensions was electro-discharge machined following the schematic shown in Fig 1. The sample was tested at $\dot{\epsilon} = 10^{-4} \text{ s}^{-1}$ and at 400 $^{\circ}\text{C}$ using an Instron ETMT 8800 testing machine that heats the sample by electrical resistance. The temperature is controlled by a thermocouple welded to the sample gauge centre. 400 $^{\circ}\text{C}$ was chosen as it is the temperature where the shot peened layer is expected to exhibit reduced ductility [33]. To guaranty both, no speckle pattern (see section 2.4) coarsening and thermal equilibrium before and during stretching, the time at temperature during tensile testing was optimized to: 10 s heating ramp at 38 $^{\circ}\text{C/s}$, 10 s at 400 $^{\circ}\text{C}$, tensile test, 400 $^{\circ}\text{C}$ held for additional 5 s after finishing the test, cooling at 38 $^{\circ}\text{C/s}$ for 10 s. All stages, except the deformation stage, were performed using force control. We interrupted the test at 1% of plastic elongation and then at successive steps

every after 0.5 % of plastic elongation until fracture, which occurred at a 4.2 %. The plastic elongation was determined by measuring the distance between two fiducial indentation marks placed right in the margins of the tested area and further verified by the average deformation values on the digital image correlation maps obtained in section 2.4.

2.4- Digital Image Correlation

We used high-resolution digital image correlation (HRDIC) to measure strain distribution at each deformation step in the green area in Fig. 1. The sectioning of the sample modifies the residual stress state. The residual stress introduced by peening is biaxial and sectioning the sample will relax the out of plane component of stress. However, the stress along the loading direction, which is relevant to the onset of plasticity studied here, will only change slightly. Therefore, although the exact stresses at which the strain localization changes will be affected, the development of plastic slip and its interaction with the residual stress will still be captured in this experiment. To make the DIC analysis possible, we first developed a fine, homogeneous distributed gold speckle pattern by remodelling a thin gold layer previously deposited on the polished sample surface. The gold layer was deposited using an Edwards S150B sputter coater for 4 minutes providing a ~40-45 nm thickness gold layer. Then, the sample was placed in the heating plate of the remodelling device described in [22,23] during 6 hours at 300 °C. During the remodelling process, water vapour flows onto the surface of the coated material and remodels the gold layer into fine speckles. In order to avoid any possible speckle coarsening during the high temperature tensile testing, the remodelled sample was heated in a furnace at 475 °C for 5 hours and air cooled to stabilise the gold

pattern. A detail of the gold speckle pattern obtained is shown in Fig. 2a together with the speckle size distribution in Fig. 2b. Due to the required stabilization heat treatment, the average speckle size was 120 nm, which is coarser than in previous studies at room temperature, where no pattern thermal stabilization is needed [25,29].

We used a FEI Magellan HR 400L FE-SEM with a theoretical resolution of ≤ 0.9 nm at <1 kV and ≤ 0.8 nm at ≥ 5 kV to take backscattered electron images of the pattern. The images were obtained at a working distance of 3.5 mm, 5 kV and 0.8 nA beam current. Mosaics of 30x15 images were used to cover $950 \times 420 \mu\text{m}^2$, an area shown area in Fig. 1). Each image contains 2048×1768 pixels and has a horizontal field of view of $43 \mu\text{m}$. The images were overlapped by 20% to enable easy stitching prior to the digital image correlation. We obtained 7 mosaics, one before tensile testing and 6 after each deformation step.

The mosaics for the un-deformed and deformed state were correlated using LaVision's digital image correlation (DIC) software (version DaVis 8.3) [34]. The correlation was performed using a sub-window size of 16×16 pixels and no overlap, which provides a spatial resolution of about 335 nm. This resolution, despite of being lower than what reached in previous studies and caused by coarser speckle size [25,29], was enough to resolve the strain associated with slip bands. In addition, it allowed us to handle the large data sets generated when covering such large areas (each mosaic was $45.5\text{k} \times 20\text{k}$ pixels in size). The correlation produces full-field in-plane displacement maps $u(x_1, x_2, 0)$ on the plane x_1x_2 with normal x_3 . Therefore, the components of the displacement gradient describing the in-plane deformation can be calculated using Eq. 1.

$$\frac{\partial u_i}{\partial x_j} = \begin{bmatrix} \frac{\partial u_1}{\partial x_1} & \frac{\partial u_2}{\partial x_1} \\ \frac{\partial u_1}{\partial x_2} & \frac{\partial u_2}{\partial x_2} \end{bmatrix} \quad [1]$$

We computed the gradient using second order accurate central differences, which ensures it is evaluated at the same points for all components and reduces the effects of displacement uncertainty on the calculation. We quantify the local strain by using the effective shear strain (γ_{eff}) as it reflects the shearing characteristic of slip and reduces the ambiguity introduced by the lack of out-plane displacement data in the HRDIC measurements. It can be calculated using Eq. 2.

$$\gamma_{eff} = \sqrt{\left(\frac{\frac{\partial u_1}{\partial x_1} - \frac{\partial u_2}{\partial x_2}}{2}\right)^2 + \left(\frac{\frac{\partial u_1}{\partial x_2} + \frac{\partial u_2}{\partial x_1}}{2}\right)^2} \quad (2)$$

We used Numerical Python [35] routines to analyse the DIC data and Matplotlib [36] to produce the visualizations. The areas at the very edge of the sample and any points unsuccessfully correlated were masked out and not considered in the analysis. These uncorrelated regions appeared as a consequence of the intrinsic difficulty of performing ex-situ high temperature tests, since the risk of contamination is higher during heating and manipulation. The raw SEM images, the HRDIC data sets and the code for reading and visualizing them can be found in [37] , [38] and [39], respectively.

3.-Results

3.1. Microstructure

The EBSD inverse pole figure (IPF) map along the out of plane direction of the shot-peened sample in the region of interest in the XY plane is shown in Fig. 3. The

non-indexed region on the right side of the maps corresponds to a fiducial indent used for locating the region of interest. From the EBSD data we obtained the IPF colour map (Fig. 3a), the grain and twin boundary map over the indexing quality image (Fig. 3b), the local kernel average misorientation values (using a 9x9 kernel size) (Fig. 3c) and (Fig. 3d) the Schmid factor (m) for $\{111\}\langle\bar{1}\bar{1}0\rangle$ slip along the testing direction (Fig. 3d). Note that the EBSD indexing was not successful in the region nearest to the sample edge (approximately 20-30 μm) due to the high degree of strain and the rounding effect of the mechanical polishing.

Grain size, excluding twins, follows a bimodal distribution with mean size ~ 20 and ~ 50 μm for each population and the material presents a random crystallographic distribution. Most of the grains contain $\Sigma 3$ annealing twin boundaries, which delimit, for a specific crystallographic orientation, a rotation of the lattice orientation of 60° about the $[111]$ axis, forming a 180° rotation of the lattice about the twin plane normal $[40,41]$. The areas named as A and B corresponds to the shot-peened and bulk regions in terms of residual stress, compressive for A and tensile for B, as described in [14]. The local plastic deformation induced by the shot-peening treatment leads to higher local misorientation values close to the top edge, visible up to a maximum depth of 40-50 nm (Fig. 3c, zone C). As expected for a face centred cubic material with a random texture the Schmid factor values for $\{111\}\langle\bar{1}\bar{1}0\rangle$ slip are high everywhere, well over 0.35, and close to 0.5 in most of the grains. This is due to the high number of available slip systems per grain, 12 in total [42].

3.2. Strain distribution

By using digital image correlation, we obtained a discretized measure of the in-plane displacement field, which was converted into values of effective shear strain (γ_{eff}) using Eq. 2. The γ_{eff} maps for successive macroscopic strain steps are presented in Fig. 4. The maps show that the strain distribution is very heterogeneous at all stages. After 1% macroscopic strain, slip is not observed in the region close to the peened surface edge, approximately 125 μm thick. However, two fine planar slip bands appear at the very sample edge (areas 1 and 2, Fig. 4a) with γ_{eff} values >0.12 , which is more than fifteen times the average strain. In the bulk below there are finely spaced planar slip bands in some grains with only a few slip bands presenting γ_{eff} values around 0.08-0.1 (area 3, Fig. 4a) while other regions show either single slip traces of low intensity ($\gamma_{eff} \sim 0.04$) or large areas with more homogeneous strain distributions (area 4, Fig. 4a). After 1.5% macroscopic strain the bands that were present previously in the peened region and the bulk become better defined and more intense while some new bands are formed. At 2% of total macroscopic strain, the initial slip bands in the shot-peened region reach $\gamma_{eff} > 0.25$ and new bands appear parallel to them, with γ_{eff} values between 0.1 and 0.2 (Fig. 4c). Additionally, high strain bands become evident containing these initial slip bands. These high strain bands propagate at 45° respect to the loading direction and penetrate the region unaffected by peening (Fig. 4c). In the strain maps at the highest macroscopic values (2.5 and 3%) and after fracture (4.2%) the highest γ_{eff} values are more homogeneously distributed along the whole region than at the initial stages of the deformation. Nevertheless, the high strain bands developed at 45° become more intense with the highest values of strain localization recorded at the sample edge, reaching γ_{eff}

>0.45 in the initial slip bands. A cursory check revealed that all slip traces are aligned with the $\{111\}$ trace, as expected, in both the shot peened region and in the bulk.

The evolution of the frequency distributions of strain values with the macroscopic strain is shown in Fig. 5. Increasing macroscopic strain displaces the distribution towards higher local γ_{eff} values. This representation shows a smooth evolution of the overall γ_{eff} values as might be expected but it does not show how the strain is localized in different regions of the material. To elucidate the variation in strain localization with sample depth, the maps were divided into 34 sections $\sim 12.1 \mu\text{m}$ thick, and the mean and median of the shear strain values were calculated. The variation in mean and median values with depth is shown in Fig. 6. At small applied deformations, there is only a small variation in the values with increasing depth, however it is clear that both decrease just below the surface and increase again at a depth of around $100 \mu\text{m}$. As the sample is strained the difference in mean strain with depth below the surface decreases and increases in the bulk of the material. An even more pronounced increase in the median value is seen in the bulk. The exception is the 4.2% straining step, which the mean strains are highest at the surface but for which the increase in median value with depth is most pronounced.

These differences in the variation of mean and median values are consequences of the different shapes of the strain distributions at the surface and in the bulk, as shown in Fig. 7. Although all distributions show a long tail, this is much more pronounced at the surface than at in the bulk, especially as the applied strain increases. As can be seen in the logarithmic plots in Figs. 7 c) and d), whereas in the bulk the tail of the distribution has a constant slope, at the surface this slope decreases with increasing strain. This

decrease in slope correspond to an increase in strain localization: a few regions show very high strains, although the average strain is lower.

This variation in strain localization can be more clearly visualized by plotting the ratio of mean to median strain, R_y , as in Fig. 8. A ratio of one represents a symmetric distribution, and although all the values are above one, the lowest values can be seen between 50 and 100 μm below the surface at 1.0% and 1.5% applied strain. At these early stages the ratio is highest in the bulk, where it increases only slightly with increasing deformation before dropping again. At the surface however, the ratio increases with increasing applied strain. Above 2.0%, the strain localization at the surface is higher than that in the bulk and is highest just below the surface. The lowest strain localization is at about 90 μm below the surface for all deformation steps. In the “bulk” of the material, strain localization is highest at low strains and deformation becomes more homogeneous as the sample is deformed further. These results demonstrate a clear effect of the shot peening process on the strain distribution. At small strains strain localization is highest just below the surface and in the bulk and at larger applied strains it is much higher at the surface.

4.- Discussion

Shot peening produces a layer of plastically deformed material at the surface, which in turn introduces a region of compressive residual stress below the surface [14]. The depth of the plastically deformed layer can be inferred from the EBSD map (labelled as region C in Fig. 3c) and is about 40-50 μm . This prior deformation would be expected to work harden the material locally and hinder plastic deformation. This is indeed seen in the deformation maps in Fig. 4, and the corresponding strain distributions in Fig. 7. There is a very slight rounding of the sample near the top edge which developed during

polishing. Although this could affect the development of local plasticity, our results show no variation in the total plastic strain near the surface region that could be related to this feature. Overall strain at the surface is lower when compared to the material in the bulk, however single sharp slip lines can be seen even after just 1.0% applied strain, as shown in Fig. 4 a). The bands intensify with further straining and eventually show the highest strain values. Thus, the plastic deformation introduced by peening hardens the material but enhances strain localization.

The variation in strain localization does not correlate directly with the zone of plastic deformation. Instead, strain localization is suppressed much further into the material as shown in Fig. 8. This profile corresponds to expected residual stress profile after shot peening, as observed, for example by Foss et al in their study on the same alloy [14]. Their stress study showed that there was insignificant stress relaxation beyond 125 μm , which is equivalent to the maximum depth of the work-hardening effects produced during the shot-peening process [7,14,43]. This suggests that local straining on loading is more noticeably affected by the residual stresses in the material than the hardening introduced by plasticity. These stresses, being compressive, delay plastic deformation (as also shown in Fig. 6) but also minimize strain localization.

Fig. 9 summarizes the effect of the stress state derived from the shot peening process and its influence on the strain distribution and heterogeneity at two macroscopic deformation stages. This figure presents a schematic of the profiles of the shot-peened residual stress and the plastically deformed region together with the profile of shear strain and mean to median ratio. Fig. 9a shows schematically the profiles at the initial deformation steps, i.e. 1-2%, and Fig. 9b corresponds to higher deformations, where the majority of the residual stress has been relaxed and close to the fracture point. The

minimum of the local strain and median to mean ratio are reached at the depth where the compressive residual stress is maximum ($\sim 100\text{ }\mu\text{m}$), which means that the strain localization is affected by the local stress state. Further deformation leads to stress release in the shot-peened region and the strain starts distributing in a more homogeneous way, comparable to what observed in the bulk.

The initial slip bands formed in the shot-peened region, just after the beginning of the plastic deformation, may act as seeds for the formation of periodic strain patterns that grow at 45° respect to the loading direction and separated around $200\text{ }\mu\text{m}$, Fig. 4. This is the case for feature 1, which is not connected to the bulk shear band at the first strain step in Fig 4.a. Additionally, such slip localization in the peened region could indeed have been enhanced stresses at the grain boundary, facilitating slip band alignment in neighboring grains and slip transfer. It does not seem likely that impurities or shot debris left on the surface during the shot-peening process could be the reason of this strain pattern, mainly due to its periodicity. Due to the difficulties on Kikuchi lines indexing in the very edge of the sample (Fig. 3), it is difficult to relate statistically their formation to a particular crystallographic orientation. Nevertheless, a detailed analysis of one of the initial slip events is presented in Fig. 10. Comparing Fig. 10a and 10c, it is evident that the first high intensity band forms along the $\Sigma 3$ twin boundary between grains 1 and 2, both grains having a very similar crystallographic orientation (Fig. 10b). This area corresponds to the deepest part of a peening dimple, where the maximum plastic deformation value is reached (zone B in Fig. 9a) In this particular case, the $\Sigma 3$ twin boundary is aligned $\sim 52^\circ$ respect to the loading direction, which is close to 45° (the angle value leading to the minimum CRSS), easing the nucleation of slip bands parallel to them, as observed in Fig. 10c and similar to what observed in fatigue tests [44]. With

further deformation (Fig. 10d), additional slip bands form parallel to the first slip band, corresponding to the $(11\bar{1})[\bar{1}10]$ slip system (Fig. 10a). Surprisingly this is not the slip system with the highest Schmid factor and still it activates earlier than the one which present the maximum m values and is only observed after 2.5 % macroscopic deformation (Fig. 4). This suggest that the initial activation of a slip system different to the most favourable one is motivated by the previous strain history and/or the residual stresses, which is aided by the disposition of the $\Sigma 3$ twin boundary. Additionally, the activation of the second slip system may be motivated somehow by the compressive stresses in the pile-up area of the peening dimple (zone A in Fig. 11a), when the compressive stresses in the zone B are partially released. Finally, at the fracture point (Fig. 10e) the initial slip band becomes thicker by the accumulation of slip events and the $(11\bar{1})[\bar{1}10]$ slip bands appear to be active in the vicinity of the twin boundary. This high strain localization around this $\Sigma 3$ boundary is similar to what reported by Stinville et al during fatigue tests in a René 88DT Ni-base superalloy, despite of the different strain history [45,46]. Additionally, studies in a AP1 Ni-base superalloy showed that crack initiation occurred preferably along twin boundaries and slip bands that intersect with the top surface at 45° [47–49]. Strains localize along these features, building up internal stresses in the material that can lead to crack nucleation when they cannot be longer accommodated. This phenomenon is critical during crack nucleation under fatigue conditions [50], where persistent slip bands (PSB) might also form aligned with the $\Sigma 3$ annealing twin boundaries [51]. Therefore, it is our contention that, despite of the essential differences between uniaxial tensile and fatigue testing, the high intensity strain allocated in these regions is a probable hot spot for crack nucleation during deformation.

High intensity strain localization not only occurs along those twin boundaries situated on the shot-peened region, as can be observed for an area allocated in the bulk in Fig. 11. In this region, those twin boundaries with angles between $\sim 30-60^\circ$ respect to the loading direction present slip bands along them at the beginning of the plastic deformation (Fig. 11b). These bands become more intense and thicker with further deformation (Fig. 11c and d) and motivate the formation of slip bands parallel to them, similar to what observed in the twin boundary in Fig. 10. This high strain localization on reloading could also be due to strain localization occurring near the twin boundaries during peening, although no evidence for it could be found using higher resolution EBSD or BSE imaging due to the high level of deformation in the peened layer. On the other hand, those twin boundaries that are almost parallel or perpendicular to the loading direction do not promote the formation of slip bands parallel to them. This fact indicates that strain localization along twin boundaries occurs in both, the shot-peened region and the bulk when they are aligned $\sim 30-60^\circ$ respect to the loading direction. Nevertheless, their only presence is not enough to describe the strain distribution observed along the depth, since their effect is similar along the whole material while the strain distribution is not. As can be deduced from Fig. 6, the local stress state through the depth also influences the strain distribution. Thus, strain localization in the shot-peened RR1000 nickel base superalloy is driven by the local stress state and its accommodation during deformation, while $\Sigma 3$ twin boundaries act as favourable slip bands nucleation sites.

5.- Conclusions

Our HRDIC results on a shot-peened RR1000 Ni-base superalloy show that the strain distributes very heterogeneously in both, the processed region and the bulk. During the initial deformation steps, up to 2.5 %, the mean strain decreases from the edge of the shot peened region towards the bulk, reaching the minimum values at $\sim 125 \mu\text{m}$. Then, the mean strain increases again up to $\sim 200 \mu\text{m}$ and remains approximately constant in the bulk. This strain profile is similar to the stress profile imposed by typical shot-peening processes, which reflect that strain localization is determined more by stress accommodation than from the purely plastic behaviour. Since the representation of the strain distribution and the mean strain distribution fail to reveal the heterogeneity in how the strain distributes, we propose using the mean to median ratio of the strain distribution to discern areas with different levels of heterogeneity. Such representation reflected the more heterogeneous distribution found on the shot-peened region than in the bulk. Both, the shot-peened region and the bulk, start accommodating deformation in high intensity slip bands formed along $\Sigma 3$ annealing twin boundaries with an angle of $30\text{-}60^\circ$ respect to the loading direction and assume the majority of the deformation. This initial slip bands promote the formation of further intragranular parallel slip bands, even if the required slip system is not the one with the higher Schmid factor. These findings show that the presence of $\Sigma 3$ annealing twin boundaries play a role on the beginning of the plastic deformation and lead the way in further strain distribution.

The strain distribution in the shot-peened RR1000 Ni-base superalloy is therefore governed mainly by the local stress state and assisted by the presence of $\Sigma 3$ annealing twin boundaries.

Acknowledgments

We would like to thank the EPSRC for funding this study through project grant EP/M005607/1, Strategic partnership in structural metallic systems for gas turbines. We are also particularly grateful to the Mechanics of Microstructures group at the University of Manchester, in particular Mr. Michael Atkinson, for the analysis software.

References

- [1] R.C. Reed, *The Superalloys: Fundamentals and Applications*, Cambridge University Press, 2006.
- [2] M.C. Hardy, B. Zirbel, G. Shen, R. Shankar, Developing damage tolerance and creep resistance in a high strength nickel alloy for disc applications, in: *Superalloys 2004 : Proceedings of the Tenth International Symposium on Superalloys*, TMS, Pennsylvania, USA, 2004: pp. 83–90.
- [3] J. Ewing, J. Humfrey, The Fracture of Metals under Repeated Alternations of Stress, *Philosophical Transactions of the Royal Society of London A*. 221 (1903) 241–253. <https://doi.org/10.1098/rsta.1903.0006>.
- [4] E.R. de los Rios, A. Walley, M.T. Milan, G. Hammersley, Fatigue crack initiation and propagation on shot-peened surfaces in A316 stainless steel, *International Journal of Fatigue*. 17 (1995) 493–499. [https://doi.org/10.1016/0142-1123\(95\)00044-T](https://doi.org/10.1016/0142-1123(95)00044-T).
- [5] S. Bagheri, M. Guagliano, Review of shot peening processes to obtain nanocrystalline surfaces in metal alloys, *Surface Engineering*. 25 (2009) 3–14. <https://doi.org/10.1179/026708408X334087>.
- [6] Y. Mutoh, G.H. Fair, B. Noble, R.B. Waterhouse, The Effect of Residual Stresses Induced by Shot-Peening on Fatigue Crack Propagation in Two High Strength Aluminium Alloys, *Fatigue & Fracture of Engineering Materials & Structures*. 10 (1987) 261–272. <https://doi.org/10.1111/j.1460-2695.1987.tb00205.x>.
- [7] S. Wang, Y. Li, M. Yao, R. Wang, Compressive residual stress introduced by shot peening, *Journal of Materials Processing Technology*. 73 (1998) 64–73. [https://doi.org/10.1016/S0924-0136\(97\)00213-6](https://doi.org/10.1016/S0924-0136(97)00213-6).
- [8] L. Wagner, Mechanical surface treatments on titanium, aluminum and magnesium alloys, *Materials Science and Engineering: A*. 263 (1999) 210–216. [https://doi.org/10.1016/S0921-5093\(98\)01168-X](https://doi.org/10.1016/S0921-5093(98)01168-X).
- [9] R. Fathallah, A. Laamouri, H. Sidhom, C. Braham, High cycle fatigue behavior prediction of shot-peened parts, *International Journal of Fatigue*. 26 (2004) 1053–1067. <https://doi.org/10.1016/j.ijfatigue.2004.03.007>.
- [10] W. Cao, M. Khadhraoui, B. Brenier, J.Y. Guédou, L. Castex, Thermomechanical relaxation of residual stress in shot peened nickel base superalloy, *Materials Science and Technology*. 10 (1994) 947–954. <https://doi.org/10.1179/mst.1994.10.11.947>.
- [11] M. Kobayashi, T. Matsui, Y. Murakami, Mechanism of creation of compressive residual stress by shot peening, *International Journal of Fatigue*. 20 (1998) 351–357. [https://doi.org/10.1016/S0142-1123\(98\)00002-4](https://doi.org/10.1016/S0142-1123(98)00002-4).
- [12] Turnbull, D.L. Rios, Tait, Laurant, Boabaid, Improving the Fatigue Crack Resistance of Waspaloy by Shot Peening, *Fatigue & Fracture of Engineering Materials*

- & Structures. 21 (2002) 1513–1524. <https://doi.org/10.1046/j.1460-2695.1998.00125.x>.
- [13] M. Frija, T. Hassine, R. Fathallah, C. Bouraoui, A. Dogui, Finite element modelling of shot peening process: Prediction of the compressive residual stresses, the plastic deformations and the surface integrity, *Materials Science and Engineering: A*. 426 (2006) 173–180. <https://doi.org/10.1016/j.msea.2006.03.097>.
- [14] B.J. Foss, S. Gray, M.C. Hardy, S. Stekovic, D.S. McPhail, B.A. Shollock, Analysis of shot-peening and residual stress relaxation in the nickel-based superalloy RR1000, *Acta Materialia*. 61 (2013) 2548–2559. <https://doi.org/10.1016/j.actamat.2013.01.031>.
- [15] G. Altinkurt, M. Fèvre, G. Geandier, M. Dehmas, O. Robach, J.-S. Micha, Local strain redistribution in a coarse-grained nickel-based superalloy subjected to shot-peening, fatigue or thermal exposure investigated using synchrotron X-ray Laue microdiffraction, *J Mater Sci*. 53 (2018) 8567–8589. <https://doi.org/10.1007/s10853-018-2144-4>.
- [16] F. Hild, S. Roux, Digital Image Correlation: from Displacement Measurement to Identification of Elastic Properties – a Review, *Strain*. 42 (2006) 69–80. <https://doi.org/10.1111/j.1475-1305.2006.00258.x>.
- [17] B. Pan, K. Qian, H. Xie, A. Asundi, Two-dimensional digital image correlation for in-plane displacement and strain measurement: a review, *Meas. Sci. Technol*. 20 (2009) 062001. <https://doi.org/10.1088/0957-0233/20/6/062001>.
- [18] A.D. Kammers, S. Daly, Self-Assembled Nanoparticle Surface Patterning for Improved Digital Image Correlation in a Scanning Electron Microscope, *Exp Mech*. 53 (2013) 1333–1341. <https://doi.org/10.1007/s11340-013-9734-5>.
- [19] N. Li, M.A. Sutton, X. Li, H.W. Schreier, Full-field Thermal Deformation Measurements in a Scanning Electron Microscope by 2D Digital Image Correlation, *Exp Mech*. 48 (2008) 635–646. <https://doi.org/10.1007/s11340-007-9107-z>.
- [20] Y. Zhang, T.D. Topping, E.J. Lavernia, S.R. Nutt, Dynamic Micro-Strain Analysis of Ultrafine-Grained Aluminum Magnesium Alloy Using Digital Image Correlation, *Metall and Mat Trans A*. 45 (2014) 47–54. <https://doi.org/10.1007/s11661-013-1805-9>.
- [21] A.D. Kammers, S. Daly, Small-scale patterning methods for digital image correlation under scanning electron microscopy, *Meas. Sci. Technol*. 22 (2011) 125501. <https://doi.org/10.1088/0957-0233/22/12/125501>.
- [22] F.D. Gioacchino, J.Q. da Fonseca, Plastic Strain Mapping with Sub-micron Resolution Using Digital Image Correlation, *Exp Mech*. 53 (2013) 743–754. <https://doi.org/10.1007/s11340-012-9685-2>.
- [23] F. Di Gioacchino, J. Quinta da Fonseca, An experimental study of the polycrystalline plasticity of austenitic stainless steel, *International Journal of Plasticity*. 74 (2015) 92–109. <https://doi.org/10.1016/j.ijplas.2015.05.012>.
- [24] D. Lunt, T. Busolo, X. Xu, J. Quinta da Fonseca, M. Preuss, Effect of nanoscale α_2 precipitation on strain localisation in a two-phase Ti-alloy, *Acta Materialia*. 129 (2017) 72–82. <https://doi.org/10.1016/j.actamat.2017.02.068>.
- [25] A. Orozco-Caballero, D. Lunt, J.D. Robson, J. Quinta da Fonseca, How magnesium accommodates local deformation incompatibility: A high-resolution digital image correlation study, *Acta Materialia*. 133 (2017) 367–379. <https://doi.org/10.1016/j.actamat.2017.05.040>.
- [26] X. Hong, A. Godfrey, W. Liu, A. Orozco-Caballero, J.Q. da Fonseca, Effect of pre-existing twinning on strain localization during deformation of a magnesium alloy,

- Materials Letters. 209 (2017) 94–96. <https://doi.org/10.1016/j.matlet.2017.07.077>.
- [27] T.E.J. Edwards, F.D. Gioacchino, H.P. Springbett, R.A. Oliver, W.J. Clegg, Stable Speckle Patterns for Nano-scale Strain Mapping up to 700 °C, *Exp Mech.* 57 (2017) 1469–1482. <https://doi.org/10.1007/s11340-017-0317-8>.
- [28] R.D. Jones, F.D. Gioacchino, H. Lim, T.E.J. Edwards, C. Schwalbe, C.C. Battaile, W.J. Clegg, Reduced partitioning of plastic strain for strong and yet ductile precipitate-strengthened alloys, *Scientific Reports.* 8 (2018) 8698. <https://doi.org/10.1038/s41598-018-26917-0>.
- [29] D. Lunt, A. Orozco-Caballero, R. Thomas, P. Honniball, P. Frankel, M. Preuss, J. Quinta da Fonseca, Enabling high resolution strain mapping in zirconium alloys, *Materials Characterization.* 139 (2018) 355–363. <https://doi.org/10.1016/j.matchar.2018.03.014>.
- [30] Y.L. Dong, B. Pan, A Review of Speckle Pattern Fabrication and Assessment for Digital Image Correlation, *Exp Mech.* 57 (2017) 1161–1181. <https://doi.org/10.1007/s11340-017-0283-1>.
- [31] G. Garcés, A. Orozco-Caballero, J. Quinta da Fonseca, P. Pérez, J. Medina, A. Stark, N. Schell, P. Adeva, Initial plasticity stages in Mg alloys containing Long-Period Stacking Ordered phases using High Resolution Digital Image Correlation (HRDIC) and in-situ synchrotron radiation, *Materials Science and Engineering: A.* 772 (2020) 138716. <https://doi.org/10.1016/j.msea.2019.138716>.
- [32] A. Orozco-Caballero, J. Quinta da Fonseca, EBSD dataset for the HRDIC strain localization study in shot peened Ni superalloy, (2021). <https://doi.org/10.5281/zenodo.4730184>.
- [33] T.J. Jackson, J. Rolph, R.C. Buckingham, M.C. Hardy, The Effect of Shot Peening on the Ductility and Tensile Strength of Nickel-Based Superalloy Alloy 720Li, in: S. Tin, M. Hardy, J. Clews, J. Cormier, Q. Feng, J. Marcin, C. O’Brien, A. Suzuki (Eds.), *Superalloys 2020*, Springer International Publishing, Cham, 2020: pp. 535–545. https://doi.org/10.1007/978-3-030-51834-9_52.
- [34] DaVis 8.3, LaVision, Germany, n.d. <http://www.lavision.de/en/company.php>.
- [35] S. van der Walt, S.C. Colbert, G. Varoquaux, The NumPy Array: A Structure for Efficient Numerical Computation, *Computing in Science & Engineering.* 13 (2011) 22–30. <https://doi.org/10.1109/MCSE.2011.37>.
- [36] J.D. Hunter, Matplotlib: A 2D Graphics Environment, *Computing in Science & Engineering.* 9 (2007) 90–95. <https://doi.org/10.1109/MCSE.2007.55>.
- [37] A. Orozco-Caballero, J. Quinta da Fonseca, RAW SEM images mosaics dataset for the HRDIC strain localization study in shot peened Ni superalloy, (2021). <https://doi.org/10.5281/zenodo.5190125>.
- [38] A. Orozco-Caballero, J. Quinta da Fonseca, HRDIC dataset of strain localization in shot peened Ni superalloy, (2021). <https://doi.org/10.5281/zenodo.4728016>.
- [39] João Quinta da Fonseca, JQFonseca/peened-ni-hrdic-analysis: v1.1, Zenodo, 2021. <https://doi.org/10.5281/zenodo.4727939>.
- [40] S. Ranganathan, On the geometry of coincidence-site lattices, *Acta Cryst, Acta Crystallogr.* 21 (1966) 197–199. <https://doi.org/10.1107/S0365110X66002615>.
- [41] O. Engler, V. Randle, *Introduction to Texture Analysis: Macrotexture, Microtexture, and Orientation Mapping*, Second Edition, CRC Press, 2009.
- [42] G.W. Groves, A. Kelly, Independent slip systems in crystals, *The Philosophical Magazine: A Journal of Theoretical Experimental and Applied Physics.* 8 (1963) 877–887. <https://doi.org/10.1080/14786436308213843>.

- [43] G.H. Majzoobi, R. Azizi, A. Alavi Nia, A three-dimensional simulation of shot peening process using multiple shot impacts, *Journal of Materials Processing Technology*. 164–165 (2005) 1226–1234.
<https://doi.org/10.1016/j.jmatprotec.2005.02.139>.
- [44] C.A. Stein, A. Cerrone, T. Ozturk, S. Lee, P. Kenesei, H. Tucker, R. Pokharel, J. Lind, C. Hefferan, R.M. Suter, A.R. Ingraffea, A.D. Rollett, Fatigue crack initiation, slip localization and twin boundaries in a nickel-based superalloy, *Current Opinion in Solid State and Materials Science*. 18 (2014) 244–252.
<https://doi.org/10.1016/j.cossms.2014.06.001>.
- [45] J.C. Stinville, N. Vanderesse, F. Bridier, P. Bocher, T.M. Pollock, High resolution mapping of strain localization near twin boundaries in a nickel-based superalloy, *Acta Materialia*. 98 (2015) 29–42.
<https://doi.org/10.1016/j.actamat.2015.07.016>.
- [46] J.C. Stinville, W.C. Lenthe, J. Miao, T.M. Pollock, A combined grain scale elastic–plastic criterion for identification of fatigue crack initiation sites in a twin containing polycrystalline nickel-base superalloy, *Acta Materialia*. 103 (2016) 461–473.
<https://doi.org/10.1016/j.actamat.2015.09.050>.
- [47] A. Boyd-Lee, J.E. King, Short fatigue crack path determinants in polycrystalline Ni-Base superalloys, *Fatigue & Fracture of Engineering Materials & Structures*. 17 (2007) 1–14. <https://doi.org/10.1111/j.1460-2695.1994.tb00768.x>.
- [48] J. Miao, T.M. Pollock, J. Wayne Jones, Crystallographic fatigue crack initiation in nickel-based superalloy René 88DT at elevated temperature, *Acta Materialia*. 57 (2009) 5964–5974. <https://doi.org/10.1016/j.actamat.2009.08.022>.
- [49] K.O. Findley, J.L. Evans, A. Saxena, A critical assessment of fatigue crack nucleation and growth models for Ni- and Ni,Fe-based superalloys, *International Materials Reviews*. 56 (2011) 49–71.
<https://doi.org/10.1179/095066010X12777205875796>.
- [50] S.R. Yeratapally, M.G. Glavicic, M. Hardy, M.D. Sangid, Microstructure based fatigue life prediction framework for polycrystalline nickel-base superalloys with emphasis on the role played by twin boundaries in crack initiation, *Acta Materialia*. 107 (2016) 152–167. <https://doi.org/10.1016/j.actamat.2016.01.038>.
- [51] M.D. Sangid, H.J. Maier, H. Sehitoglu, The role of grain boundaries on fatigue crack initiation – An energy approach, *International Journal of Plasticity*. 27 (2011) 801–821. <https://doi.org/10.1016/j.ijplas.2010.09.009>.

Figures

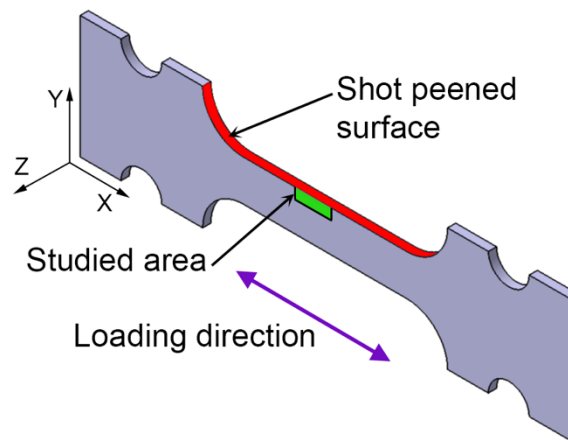


Figure 1: Schematic of the sample. The sample was shot-peened in the XZ plane, along the region highlighted in red. The studied area is the cross plane respect to the shot-peened plane, the XY plane, in an area of $950 \times 420 \text{ m}^2$, highlighted in green.

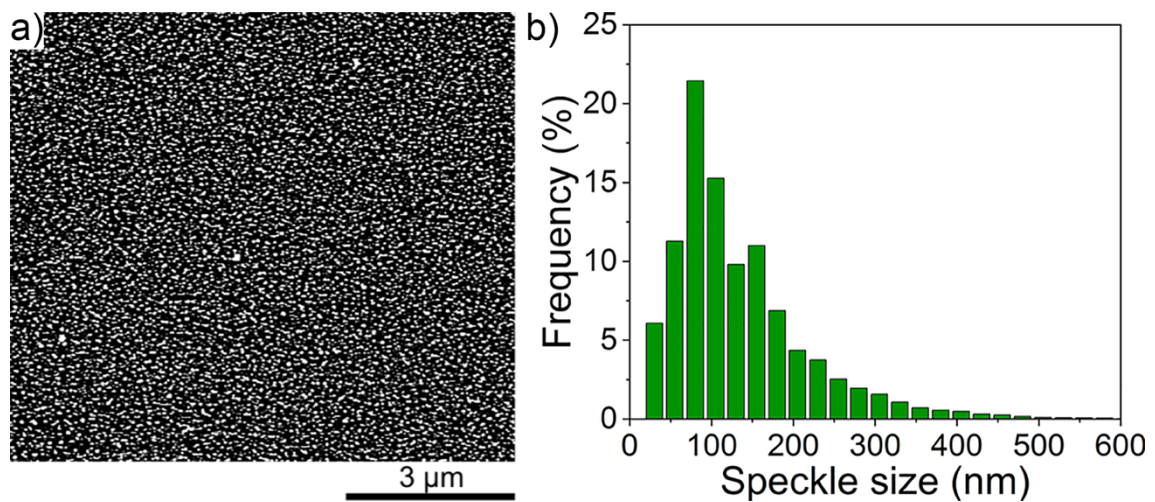


Figure 2: Gold speckle pattern. a) Backscattered electron image showing the fine and homogeneously distributed gold speckle pattern developed on the sample XY plane after water-

vapour remodelling and stabilisation. b) Pattern size distribution. The average speckle size was 120 nm.

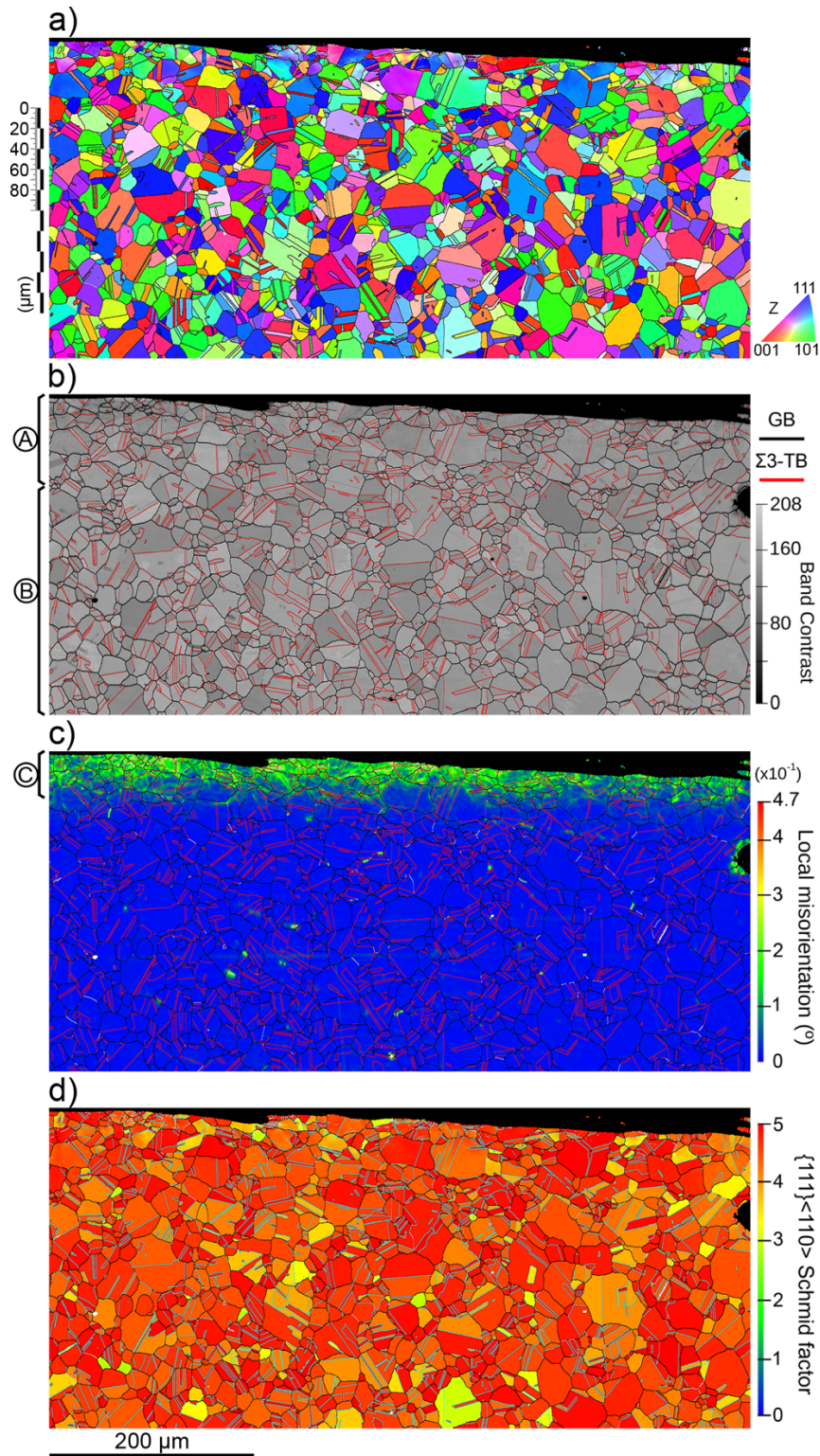


Figure 3: Microstructural characterization of the region of interest. (a) EBSD map represented using IPF colours respect to the observation Z-axis. This representation does not differentiate the character of the boundaries. (b) Band contrast map including grain boundaries (black) and $\Sigma 3$ twin boundaries (red). (c) Local misorientation or KAM (kernel average misorientation) map using a 9x9 kernel size. (d) Distribution of the Schmid factor (m) for slip along $\{111\}\langle 110\rangle$ when loading along the X-axis (horizontal dimension of the figure).

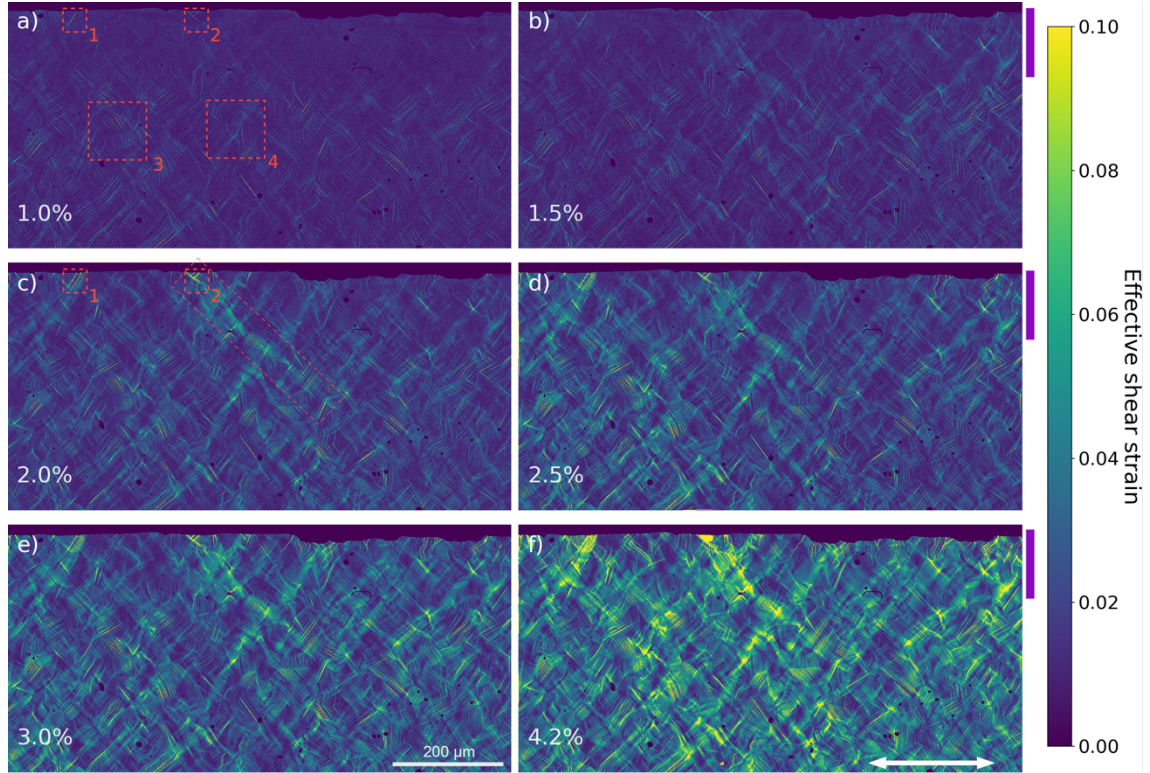


Figure 4: HRDIC maps. Effective shear strain values at increasing levels of applied uniaxial strain: (a) 1.0%, (b) 1.5% (c) 2.0%, (d) 2.5%, (e) 3.0% (f) failure at 4.2%. Loading direction is indicated by the white arrow while the depth of the peened volume is marked by the perpendicular purple line.

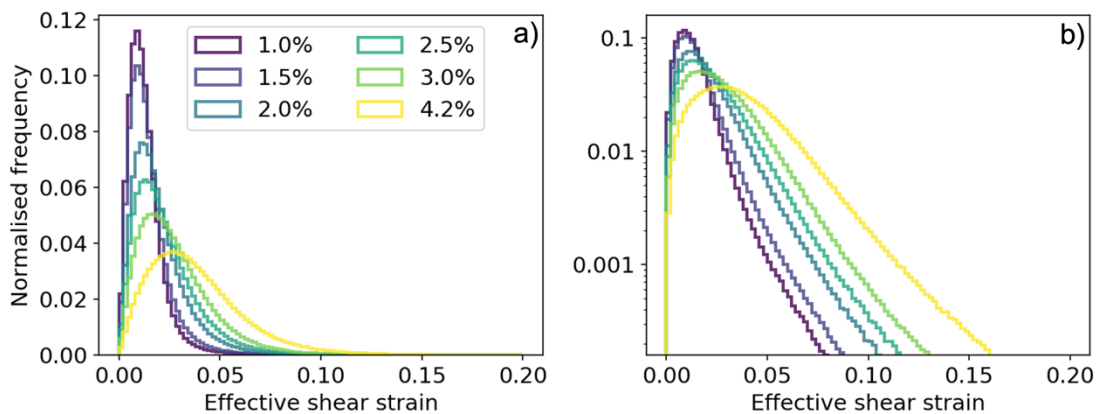


Figure 5: Strain distribution. a) Distribution of effective shear strain values across the whole region of interest at the six macroscopic deformation steps. b) Additional plot provides the normalized frequency in a logarithmic scale for evidencing the distributions tails. A decrease in slope of the tail correspond to an increase in strain localization.

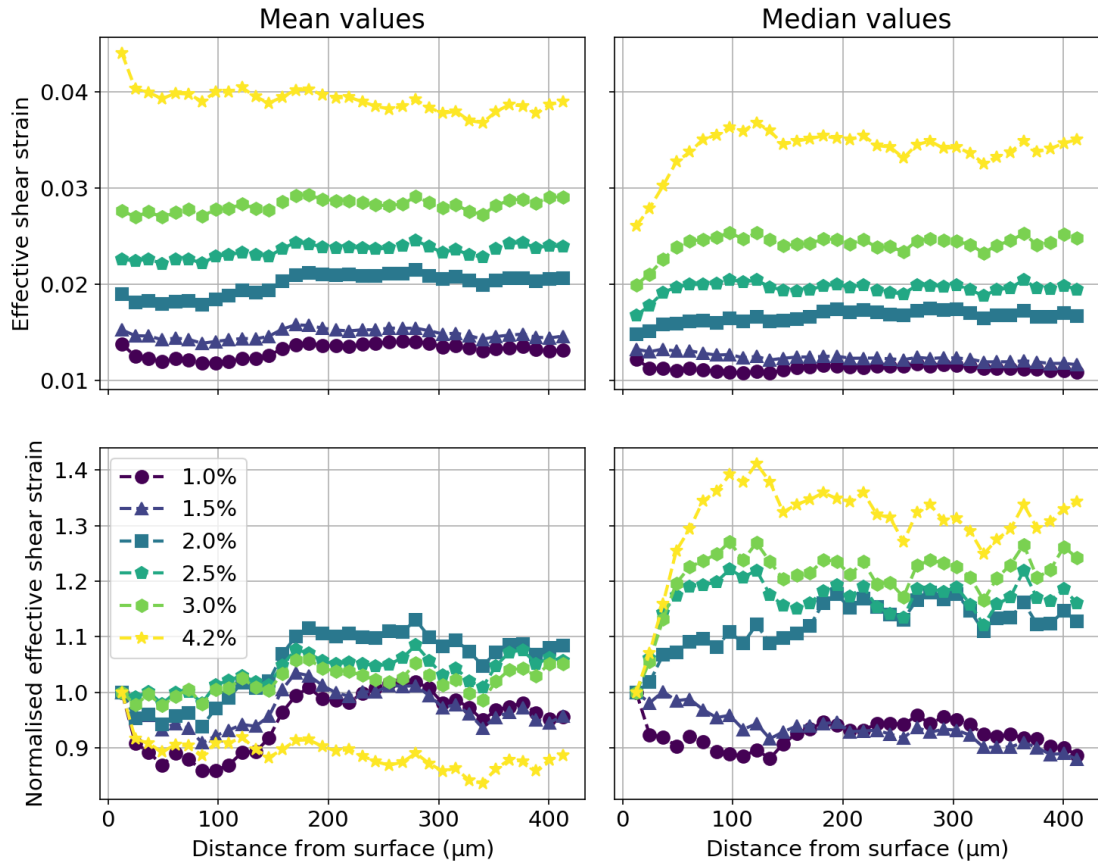


Figure 6: Strain variations. Change in mean effective shear strain calculated over 12 slices at different distances from the surface.

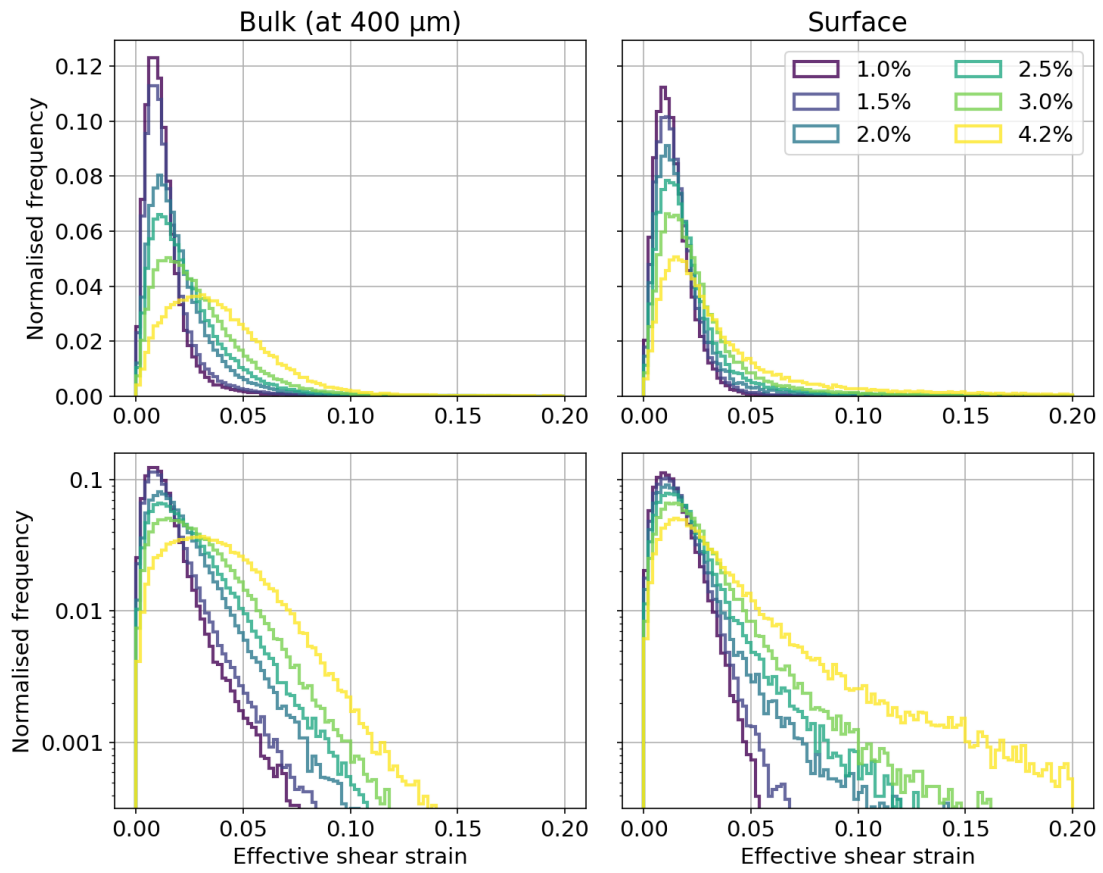


Figure 7: Surface vs. bulk. Normalized strain distributions for the slice at the surface and one in the bulk, at 400 μm from the surface.

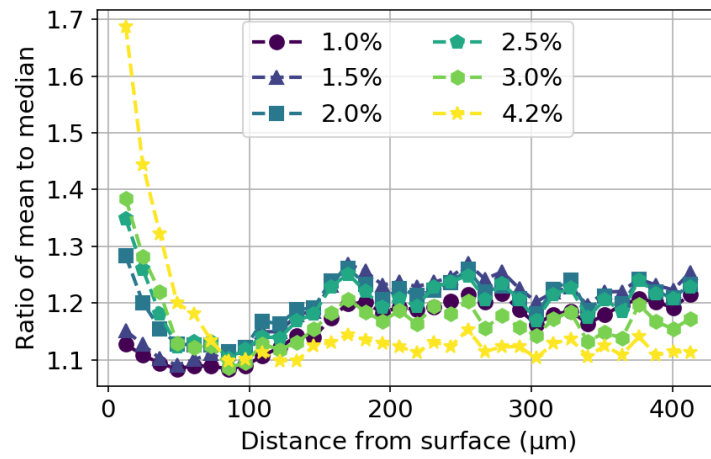


Figure 8: Strain localization. Ratio of mean to median effective strain measure as a function of distance to the surface.

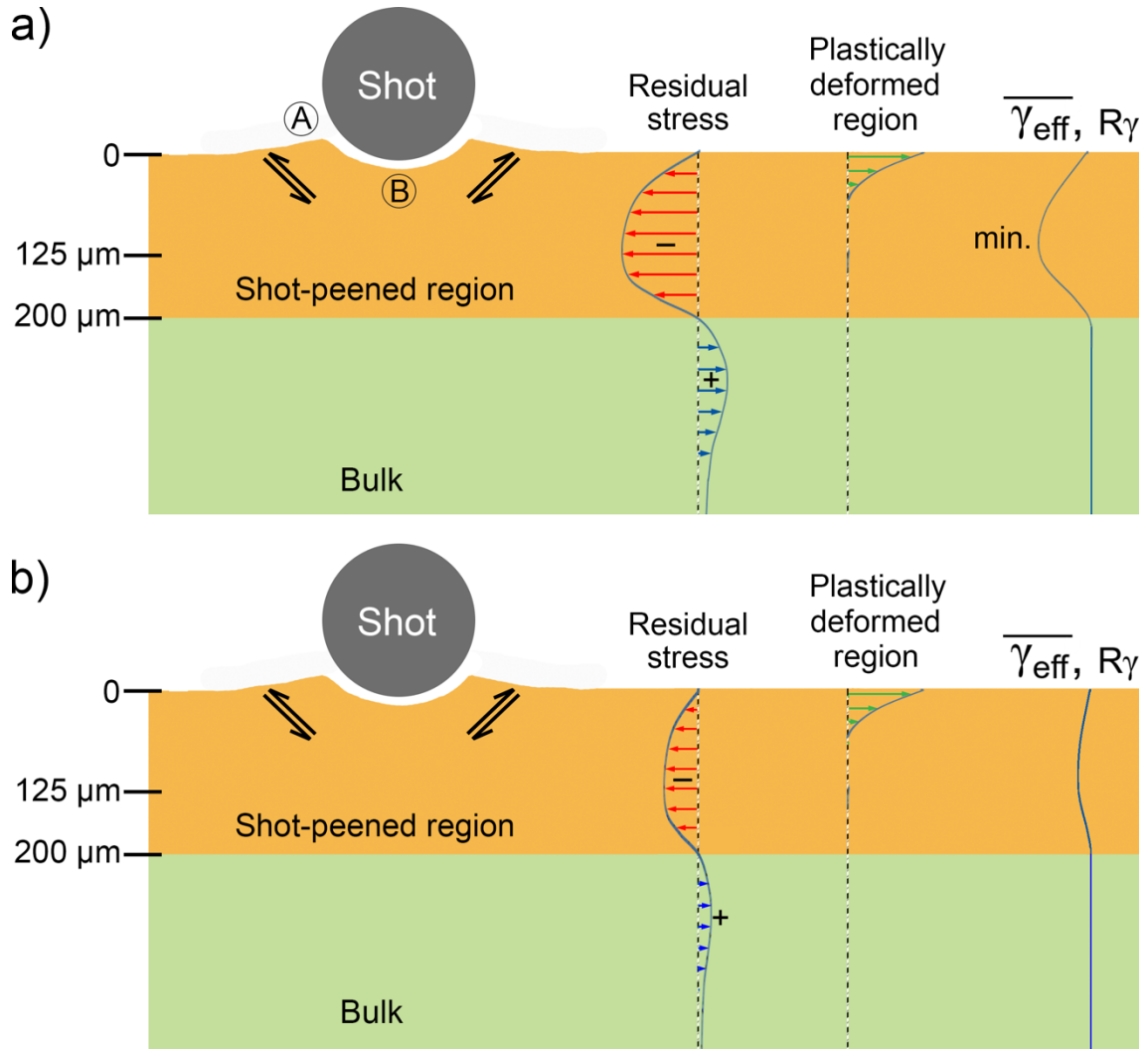


Figure 9: Local stresses and strain distribution profiles. The shot peening process induce a plastically deformed region and a compressive stress profile along the depth of the sample. The local stress state gradient determines the way the local strain distributes, as revealed by the strain depth profiles, especially at (a) the first deformation steps (up to 2.5%). Once the residual stress relaxes during further deformation (over 2.5%), the strain distribution becomes more homogeneous.

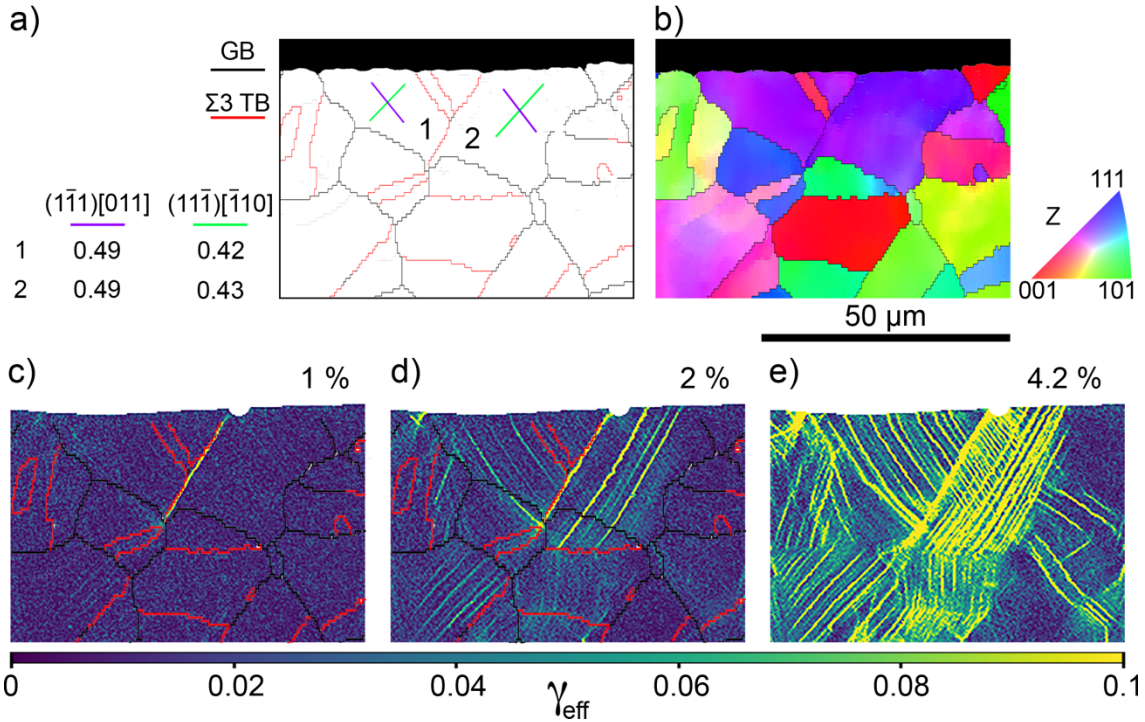


Figure 10: Area of first nucleation of slip bands in the shot-peened region. a) In the boundary character map we include the traces for the slip systems with Schmid factor higher than 0.35 in grains 1 and 2. The table presents the m values for the two higher Schmid factor slip systems. b) The EBSD map shows the crystallographic orientation of the grains respect to the observation axis (Z). c) After a 1% of macroscopic plastic deformation, the HRDIC map shows a high intensity band formed along the $\Sigma 3$ twin boundary between grains 1 and 2. d) After 2% more slip bands form within both grains. In the case of grain 2 they are aligned with the initial one, corresponding to the activation of the slip system with the second higher m factor value. e) At the fracture deformation step the initial band is thicker than at previous strain steps. Within both grains a higher density of slip bands is observed and in the case of grain 2 a second slip system is active, which corresponds to the higher m factor value. Note: the apparent difference in background noise in the strain map compared to other figures is due to the higher magnification used here.

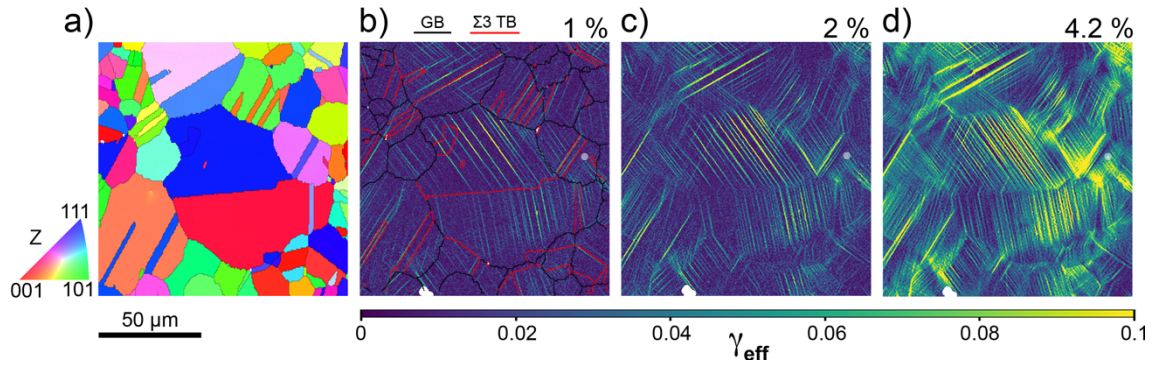


Figure 11: Slip band distribution in an area within the bulk. The a) EBSD map present an area with a random crystallographic orientation distribution. After b) 1% of macroscopic deformation some slip bands are formed along $\Sigma 3$ twin boundaries, while some other slip bands form within the grains. Their intensity and density keep increasing with further deformation c). At d) the fracture deformation step the slip bands along the $\Sigma 3$ twin boundaries tend to become thicker and accumulate more deformation than the slip bands within the grains.